

ARTICLE

<https://doi.org/10.1038/s42005-019-0160-6>

OPEN

Laboratory investigation of particle acceleration and magnetic field compression in collisionless colliding fast plasma flows

D.P. Higginson^{1,2}, Ph. Korneev ^{3,4}, C. Ruyer^{1,5}, R. Riquier^{1,5}, Q. Moreno⁶, J. Béard⁷, S.N. Chen^{1,8}, A. Grassi¹, M. Grech¹, L. Gremillet⁵, H. Pépin⁹, F. Perez¹, S. Pikuz ^{3,10}, B. Pollock², C. Riconda¹, R. Shepherd², M. Starodubtsev¹¹, V. Tikhonchuk ^{6,12}, T. Vinci ¹, E. d'Humières¹² & J. Fuchs ^{1,11}

In many natural phenomena in space (cosmic-rays, fast winds), non-thermal ion populations are produced, with wave-particle interactions in self-induced electromagnetic turbulence being suspected to be mediators. However, the processes by which the electromagnetic energy is bestowed upon the particles is debated, and in some cases requires field compression. Here we show that laboratory experiments using high-power lasers and external strong magnetic field can be used to infer magnetic field compression in the interpenetration of two collisionless, high-velocity (0.01-0.1c) quasi-neutral plasma flows. This is evidenced through observed plasma stagnation at the flows collision point, which Particle-in-Cell (PIC) simulations suggest to be the signature of magnetic field compression into a thin layer, followed by its dislocation into magnetic vortices. Acceleration of protons from the plasma collision is observed as well. As a possible scenario, with 1D and 2D PIC simulations we consider a compression of the vortices against dense plasma remnants.

¹LULI - CNRS, Ecole Polytechnique, Université Paris-Saclay, Sorbonne Université, CEA, F-91128 Palaiseau Cedex, France. ²Lawrence Livermore National Laboratory, Livermore, CA 94440, USA. ³National Research Nuclear University MEPhI, 115409 Moscow, Russian Federation. ⁴P.N. Lebedev Physical Institute (LPI), RAS, 119991 Moscow, Russian Federation. ⁵CEA, DAM, DIF, F-91297 Arpajon, France. ⁶ELI-Beamlines, Institute of Physics Academy of Sciences of the Czech Republic, 252 41 Dolní Břežany, Czech Republic. ⁷LNCMI, UPR 3228, CNRS-UGA-UPS-INSA, F-31400 Toulouse, France. ⁸ELI-NP, "Horia Hulubei" National Institute for Physics and Nuclear Engineering, 30 Reactorului Street, RO-077125 Bucharest-Magurele, Romania. ⁹INRS-EMT, 1650 bd. L. Boulet, Varennes, QC J3X 1S2, Canada. ¹⁰Joint Institute for High Temperatures, RAS, 125412 Moscow, Russian Federation. ¹¹Institute of Applied Physics, 46 Ulyanov Street, 603950 Nizhny Novgorod, Russian Federation. ¹²CNRS-CEA, CELIA, UMR5107, University of Bordeaux, F-33405 Talence, France. Correspondence and requests for materials should be addressed to J.F. (email: julien.fuchs@polytechnique.fr)

Non-thermal ion populations are observed to be produced in many space and astrophysical environments (ref. ¹ and refs therein), from the solar wind² to the expanding envelope of supernova remnants, in which the acceleration of high-energy cosmic-rays is suspected to take place³. In most cases, diffusive shock acceleration (DSA)^{4–6} is invoked as a likely scenario, as e.g., following Chandra observations of supernova remnants⁷. The basic model of this process is that of a collisionless shock, in which dissipation is provided through wave-particle interactions as a result of microscale plasma instabilities^{6,8,9}. Scattering of the energetic particles across the shock front gives rise to a population of suprathermal particles, whose unstable interaction with the upstream plasma flow sustains the turbulence generation, and hence the acceleration process. DSA could also take place in the interaction of relativistic, magnetized¹⁰ outflows stemming from astrophysical sources (e.g., following a supernova explosion) with ambient magnetic field and matter. The possibility for DSA to be efficient enough to produce observed cosmic-rays remains the subject of intense debate, and alternative scenarios of acceleration have been postulated, depending on the magnetic field orientation or the shock velocity, although most notably acceleration is expected in quasi-perpendicular shocks¹¹. Particle acceleration, however, can also occur in the absence of shockwaves, e.g., during reconnection events¹² or the expansion into vacuum of a magnetized relativistic plasma. The latter process, referred to as diamagnetic relativistic particle acceleration (DRPA)^{13,14}, proceeds through the generation of a strong electromagnetic pulse at the plasma front, which accelerates particles, via the ponderomotive force, to relativistic energies. Nonetheless, the generation of non-thermal ions in such conditions has not yet been observed in the laboratory, and remains a puzzle, since none of these processes have been evidenced directly.

Now, due to the rapid advancement of high-power lasers and of associated precise diagnostics techniques, there is finally the capacity to access, via laboratory experiments, regimes that are analogous to the potential astrophysical drivers of this acceleration and thus evaluate the efficiency of some of the proposed acceleration mechanisms. In fact, such work has already resulted in better understanding of the interaction of counter-streaming high Mach-number unmagnetized flows^{15–19}, how this leads to the growth of the two-stream or Weibel instability^{20,21} and the development of the initial stages of collisionless shocks²².

Here, we perform laboratory experiments using high-power lasers to generate interpenetration of two collisionless, high-velocity (0.01–0.1c) plasma flows within a strong external magnetic field. We observe plasma stagnation at the mid-point between the two flows; Particle-in-Cell (PIC) simulations suggest this to be the consequence of magnetic field compression into a thin layer, followed by its dislocation into magnetic vortices. Acceleration of protons from the plasma collision is observed experimentally. To understand this acceleration, 1D and 2D PIC simulations investigate the compression of the magnetic vortices against dense plasma remnants.

Results

Experimental setup. Here, to explore the ability of fast plasma flows to compress an ambient magnetic (B) field, and to accelerate particles in regions of high magnetic fields, we generated two counter-streaming plasmas (see Methods). These plasmas are produced following the irradiation of the external surfaces of two opposing Al solid targets using two coincident, short-pulse (0.65 ps), high-intensity ($7 \times 10^{19} \text{ W cm}^{-2}$) lasers of the Titan laser at the Jupiter Laser Facility (Lawrence Livermore National Laboratory, USA), aligned in time to within the laser pulse duration,

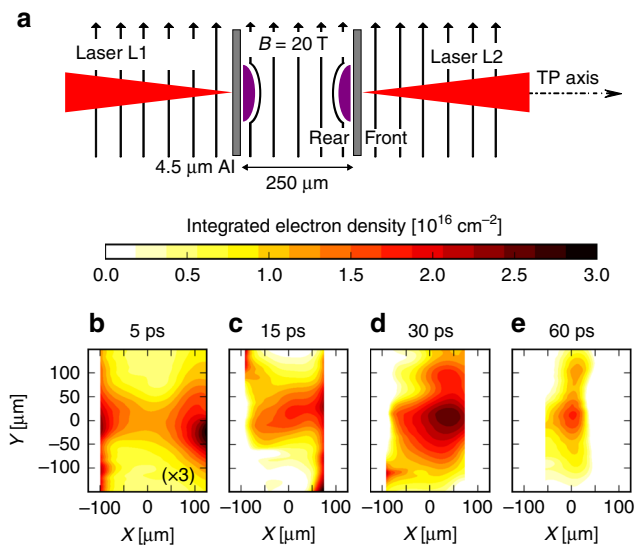


Fig. 1 Experimental evidence for late-time plasma stagnation when colliding two fast plasmas in an ambient magnetic field as a signature of magnetic field compression. **a** Schematic of the experimental set-up. Two lasers irradiate two solid targets, accelerating two quasi-neutral, fast flows (electrons and ions, which are mostly protons) from the rear surface, which expand into each other in the imposed 20 T magnetic field. The axis of the Thomson Parabola (TP) is shown and the interferometry diagnostic axis is into the page. **b–e** Electron density in the plasma, integrated along the line of sight (and hence in units of cm^{-2}), as measured by the interferometer, at different times from the laser interaction. The frame (**b**), corresponding to 5 ps, uses a colorscale that represents 3 times more density than that of the other frames in order to better highlight the plasma profile at this time

hereafter denoted as L1 and L2 and as shown in Fig. 1a. The high-energy (multi-MeV) quasi-neutral ion-electron plasmas, in which protons are the predominant species²³, are produced from each target via the target normal sheath acceleration (TNSA) mechanism²⁴. As a result, the kinetic energies of the ions in each flow are characterized by an exponentially decaying distribution function. The acceleration and interpenetration of the two plasma streams take place in an externally applied 20 T magnetic field perpendicular to the flow axis produced using a pulsed Helmholtz coil (20 T at the center, decaying to 0 T at 40 mm away, see Methods). Numerical simulations^{25,26} have shown that a perpendicular B-field tends to amplify the magnetic structures that develop during the plasma collision, hence potentially enhancing the particle energization.

We verified that applying the external magnetic field by itself did not affect strongly the TNSA mechanism. A comparison of the proton spectra accelerated from a single foil obtained on axis with and without the applied magnetic field is shown in Supplementary Note 1. The high-energy cutoff is unchanged, which suggests that the ions at the edge of the colliding plasmas are weakly affected by the B-field. We also underline that the flows are of higher velocity (0.01–0.1c, deduced from the ion spectra, see Supplementary Fig. 1, and the detailed discussion in ref. ²⁷) than those used in previous laboratory studies using lasers^{15–17,19–21,28}, and that they are highly non-collisional, as astrophysical flows. In our setup, the collisional mean-free-path (due to ion-ion collisions) is $\geq 10^8 \mu\text{m}$ ²⁷, while the separation between the two targets is varied between 250 and 500 μm .

Measurement of the electron density evolution. To measure the temporal evolution of the electron density profile in the plasma between the two targets, a Mach-Zehnder interferometer, using a

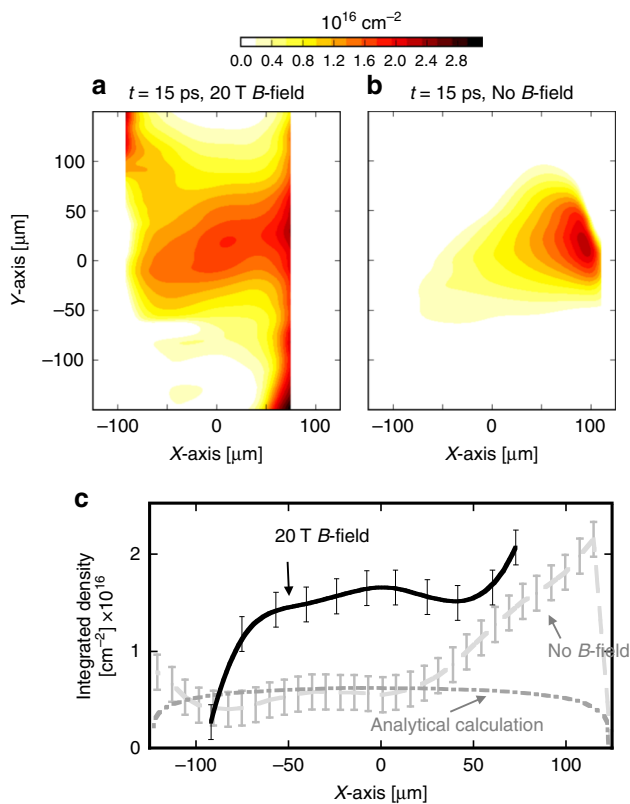


Fig. 2 Integrated electron density measurements using the interferometer at 15 ps after the laser irradiation with and without applying the external magnetic field. Panels (a) and (b) show cases with and without an applied B-field (panel (a) is the same image as the one shown in Fig. 1c, just reported here for ease of comparison). Panel (c) plots longitudinal lineouts (at $y = 0$) for both cases (with B: solid black line, without B: dashed gray line), as well as the analytical calculation (dotted-dashed gray line) that corresponds to Supplementary Fig. 5d and that would result from a simple linear overlap of the two TNSA plasmas expanding from both targets. Note also that the without B-field case corresponds to Fig. 11 of ref. 27. The calculation of the error bars is discussed at the end of the “Experiments” section of the Methods

probe laser, was aligned perpendicular to the targets and the B-field (i.e., out of the page in Fig. 1). As detailed in ref. 27, the promptly accelerated²⁹ plasmas have a density around 10^{18} cm^{-3} , are traveling around $0.01\text{--}0.1c$ ($\sim 10^8\text{--}10^9 \text{ cm s}^{-1}$) and are expected to have electron temperatures in the 1–100 keV range. Images and profiles of the integrated density between the targets are shown at times of 5, 15, 30, and 60 ps in Fig. 1 when the magnetic field is applied.

Figure 1b–e shows the evolution of the plasma electron density inside the counter-flowing plasmas. We observe that a stagnating electron structure forms in the central region a few ps after the encounter of the two flows. At early times (Fig. 1b), as expected²⁷ (see also Supplementary Fig. 5a, c), the plasma has a density profile with a peak at the target surfaces and then decays towards the center of the two targets. However, at later times (Fig. 1c–e), the density profile develops a density bump on axis that persists until 60 ps. Such density increase is not observed without an applied magnetic field. This can be seen in Fig. 2a, b which compares the electron density maps obtained at 15 ps after the laser irradiation with and without an external magnetic field, the latter having been previously reported in ref. 27. In both cases, we have the two targets irradiated by the two lasers. Figure 2c plots lineouts for the two cases along x at the centerline (i.e., $y = 0$).

Without a magnetic field, there is a monotonic decrease in the electron density from the right-side target to the center. This contrasts with the plateau observed in the magnetized case. Note also that the measured density without an external magnetic field corresponds quite well to the one expected from a linear overlap of the two plasmas flowing from both targets, the calculation of which is detailed in Supplementary Note 2, and which is represented by the dotted-dashed gray line in Fig. 2c.

We also note that the density bump observed on axis at later times (Fig. 1c–e) is not expected to take place as the result of the simple overlap of the plasma flows, as detailed in Supplementary Note 2, in which case we would expect a flat integrated density profile at the center, with falling off edges on both sides, as illustrated also in Fig. 2c²⁷.

We expect that, especially at early times, the plasma should have high magnetic Reynolds numbers; as a result, the magnetic fields should be frozen into the plasma expansion, and thus advected along with the plasma flows. This behavior is consistent with the early dynamics observed in our Particle-In-Cell simulations (see Methods).

2D Particle-in-Cell simulations of magnetic field compression.

The simulations were performed in 2D, with spatial scales corresponding to the smallest separation distance used in the experiments between the two targets (i.e., 250 μm), a focus on the interaction zone and with truncated density and velocity profiles due to computational limitations (at higher densities and lower velocities). In the magnetized case, the two initially unmagnetized counterpropagating plasmas expand into the vacuum between the targets, filled with the external magnetic field. At this stage, the magnetic field is expelled by the edge of the expanding plasmas because the magnetic diffusion time $\sim \sigma L^2/c^2 \sim 10^{-2} \text{ s}$ (where σ is the plasma conductivity, L is the characteristic length scale, and c is the speed light) is much greater than the characteristic expansion time of tens of ps. As a result, at the center of the system, a layer of compressed magnetic field is formed. Only a thin layer of electrons at the expansion fronts is magnetized³⁰ but this does not prevent the formation of the compressed magnetic field layer up to twice the background magnetic field value (up to 50 T, as inferred from the simulations). Following this, a surface instability develops, as detailed in ref. 31, because of the appearance of surface currents linked to the reduced electron Larmor radius in this zone. This results in the creation of magnetized low-density vortices inside the higher-density unmagnetized plasma, as shown in Fig. 3a–d, where one of these vortices is visible. The slower ions arriving at later times and continuing to stream from both targets, and that would have otherwise been reflected in the high magnetic field compressed region, can more easily propagate in the low magnetic field regions surrounding the distributed magnetic vortices (see Fig. 3e–h).

The propagation of the lower-velocity ions through the central region is linked with a lower thermal pressure which allows the magnetic vortices to diffuse and drift, and indeed at later times, these vortices are seen in the simulations to drift longitudinally out of the simulation box. This diffusion of the magnetic vortices, in turn, affects the propagation of the lower-velocity ion flows which follow the paths presenting the lowest magnetic fields (see Fig. 3e–h). This interplay leads to a plasma stagnation zone at the center of the simulation box where a region with lower magnetic fields is formed (see Fig. 3i), which is consistent with the experimental observations shown in Fig. 1. The simulated maximum density in the stagnation zone is lower than in the experiments. This is due to the fact that the simulations use truncated velocity distributions (at low velocities), and hence underestimate the late-time achievable thermal pressure and

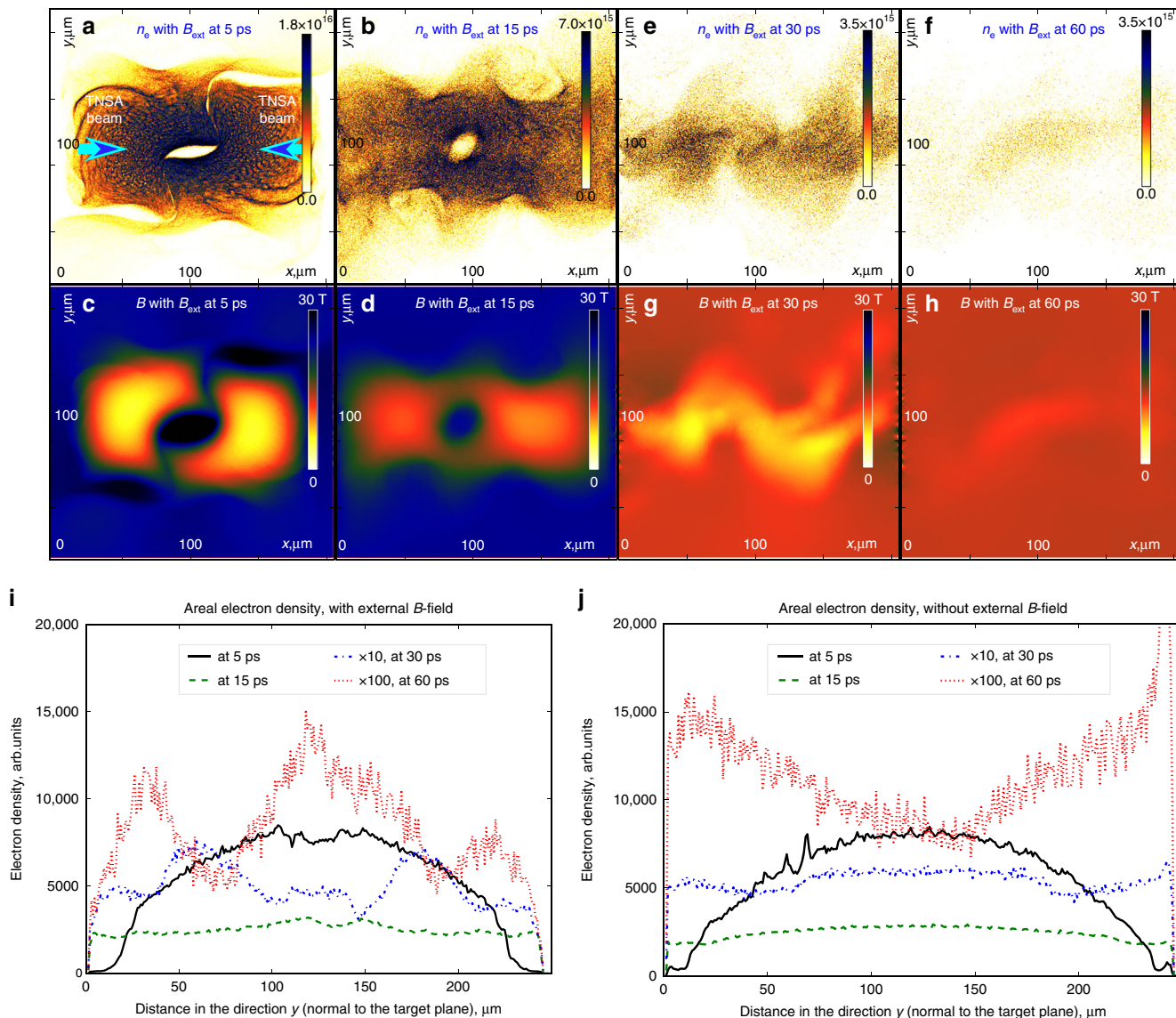


Fig. 3 Particle-in-Cell simulations of the plasma and magnetic field evolution in the collision of two plasmas in an ambient magnetic field. Electron density (a, b, e, f) and magnetic field (c, d, g, h) pseudo-color images from the Particle-in-Cell simulations of two symmetric colliding plasma flows at different time moments after the beginning of the simulation (from left to right: 5, 15, 30, 60 ps), in the case where a uniform 25 Tesla external magnetic field is applied, note this is 25% higher than the 20 T used experimentally. Areal electron densities (integrated in the x direction) in the cases with (i) and without (j) applied magnetic field

stagnation level. It is important to note that this stagnation in the central region is linked in the simulations to longitudinal gradients of the magnetic field which are generated due to the longitudinal drift of the magnetic vortices resulting from the magnetic barrier evolution. Note also that the vortices cannot experimentally be resolved as the interferometer diagnostic is line-integrated along a plane, smoothing the data and decreasing the effective spatial resolution. We have further verified that in the simulations, as in the experiment, the stagnation of the colliding plasmas at late times does not occur without the external B-field (see Fig. 3j) and Supplementary Note 3).

Experimental observation of proton energization. Concomitantly with the observation of plasma stagnation in the case where an external magnetic field is applied, we observed in the experiment a clear signature of proton energization as emerging from the colliding plasmas. Figure 4 shows different energy spectra from the Thomson Parabola spectrometer³² used for that

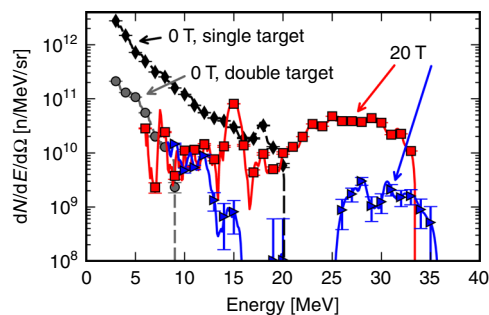


Fig. 4 Evidence for proton energization in the collision of two fast plasmas in an ambient magnetic field. Proton spectra as recorded by the Thomson Parabola. Several spectra corresponding to unmagnetized shots are shown: a single foil irradiated with the L1 laser beam only (diamonds) and two foils irradiated with both beams (circles). Two duplicate shots with both foils and a 20 T imposed B-field (squares, triangles) are also shown. Error bars correspond to the noise level on the image plate diagnostic

measurement. The shots without an applied magnetic field show exponentially decaying energy spectra, as expected from the TNSA acceleration mechanism. The single target shot refers to the case where a single target was irradiated by laser L1, allowing the observation of the rear-surface protons from a single target to be observed alone. The double target shot without B-field uses both targets and both lasers. The double target shot is much lower in both peak energy and number than the single target shot. The reason for this could be that the double target shot integrates both the rear-surface emission induced by L1, but as seen through the target irradiated by L2, as well as the front-surface emission from that target which faces the diagnostic (rear and front are defined for clarity in Fig. 1a). This front-surface emission is well known to be less effective at accelerating protons^{23,33}. Note also that we have tested in a prior experiment that, without L2 and without magnetic field, the protons stemming from the target irradiated by L1 only would not be spectrally affected by the other target for the gaps used in this experiment as the TNSA acceleration of the protons would be already completed³⁴. A few reasons could account for the rear-surface accelerated protons to be overshadowed in the diagnostic by the front-emitted ones. Protons could be collisionally scattered in the target; using the Monte-Carlo code TRIM³⁵, we verified that over 99% of the protons passing through a 4.5 μm Al foil would be scattered out of the diagnostic if the target was cold, which is a reasonable assumption since the protons will cross the gap between the two targets in only a few tens of ps, at which time the solid target will not hydrodynamically disassemble, as this would rather take place of ns. We also note that the presence of magnetic fields close to the target surface^{36,37} could deflect the protons but would have an overall focusing effect close to the axis.

The peak energies observed from the rear of the L2 without the external B-field were limited to 9 (with the two targets) and 20 MeV (with one target), both with an uncertainty of 20%. Conversely, in the shots with an external B-field and only in the case of the colliding plasmas, the maximum proton energy increases up to 35 MeV, which corresponds to an energy gain of 2–3 times in the magnetic interaction. As mentioned above, we tested that applying the large scale external magnetic field neither modified the TNSA initial expansion nor prevented the high-energy part of the beam from escaping the coil (see Supplementary Fig. 1). Interestingly, we find that these protons are not inhibited as they travel through the L2 target, unlike in the unmagnetized two-foil case. This may suggest that either these protons originate at higher energy, or that they follow a different trajectory to avoid electric or magnetic fields.

Discussion

In the PIC simulations discussed above, we did not observe significant energy redistribution or particle acceleration following the magnetic vortices formation and plasma flow through them as they drift away from the center of the system. As observed in Fig. 3, the magnetic vortices drift from the collision region at a measured characteristic velocity of $\sim 3 \times 10^8 \text{ cm s}^{-1}$. After several tens of ps, these vortices exit the simulation box and are not followed anymore. Moreover, we point out that as mentioned above, these simulations could not integrate the TNSA source targets nor the full TNSA expanding plasma density profiles.

An interesting new scenario for the source of the ion acceleration resulting from the collision observed in the experiment is supported by simulations, and results from the evolution of the magnetic vortices, formed during the breakup of the compressed magnetic barrier at the center of the colliding plasmas, and which interact with the remaining solid-density targets at the system edge. Colliding with these high density remnants, the magnetic

vortices could be compressed due to the impossibility for the magnetic field to fully penetrate into the dense and cold regions; only a fraction of the magnetic field penetrates, corresponding to the pressure equilibrium between the cold plasma region and the incoming TNSA plasma flow toward it, in between which the magnetic field is compressed. We tested this in separate 1D PIC simulations (detailed in Supplementary Note 4), looking at the evolution of one part of the system comprising the magnetic field of the vortex, the TNSA plasma flowing toward it and one of the solid-density targets. We observed that the electrons within the TNSA plasma continuously flowing through the dissolved magnetic barrier can be trapped and accumulated in the compressed magnetic field. Following this, an electrostatic potential builds up, leading to an ambipolar electrostatic field which in turn can accelerate the cold ions present in the density gradients of the high density remnants. This dynamics takes place very rapidly: simulating only 1 ps duration after the edge of the TNSA flow arrives at the original position of the opposite target, we observe that the acceleration process is already saturated. The saturation takes place as the expanding high-density remnant experiences a reduced internal plasma pressure, no longer able to maintain the magnetic field compression and the associated electron confinement. We note that protons originating from the contaminant layers²³ present on the target surface can be accelerated this way as they have not been fully depleted in the initial TNSA plasma flows. The TNSA flow containing $\sim 10^{13}$ protons is measured to stem from a 0.3 nm layer of the surface contaminants (assuming a 200 μm wide sheath field³⁸) which has been measured to be usually 1–2 nm thick²³. It is important to note that in order for this mechanism to be efficient and accelerate protons to high energies, the magnetic field should not be too strong and peaked in space otherwise the electrostatic acceleration is too strong early on, leading to a quick target expansion and a fast disruption of the acceleration. With our present simulation capabilities, it is difficult to test a realistic dynamics of the TNSA colliding flows and of the subsequent magnetic field compression and evolution, and hence to foresee which strength and distribution the drifting magnetic vortices could experience as they reach the solid targets. However, we can state that we tested that to achieve 10 MeV acceleration, a magnetic field of the order of 500 T is required, setting a high constraint for the magnetic field evolution. This value is much higher than the one predicted by our 2D PIC simulations shown in Fig. 3, but a more realistic setup (including the whole TNSA process, 3D in space, etc.), currently out of our simulation capability, may result in an additional evolution of the field. The 2D magnetic vortices observed would become magnetic tubes that could be subject to additional twisting, with a possibility of interactions between these tubes, leading in further amplification of the associated magnetic fields^{39,40}.

The presently reported first evidence of magnetic field compression and ion energization points to an alternative mechanism for ion acceleration with respect to the presently invoked DSA and DRPA. It opens the way to the study of astrophysically relevant processes of fast flows like collisionless magnetic field compression or high energy particle production, the prospect of which will likely be strongly strengthened by the upcoming opening of multi-PetaWatt facility.

Methods

Experiments. The Titan laser, used in this study, is located at the Jupiter Laser Facility of the Lawrence Livermore National Laboratory. The laser was used in a split-beam configuration producing the L1 and L2 laser beams, with each beam containing 60 J. The beams have a wavelength of 1054 nm, have a duration of 650 fs and were focused to hit the aluminum targets at 60° using $f/3$ off-axis parabolas to form a 10 μm in diameter focal spot. The target thickness was 4.5 μm , we verified that proton acceleration was not inhibited by the laser prepulse by shooting

different target thicknesses (down to 2 μm) and monitoring the on-shot prepulse energy. The two beams were aligned in time by optimizing the interference pattern using a glass slide to image the pulsed beams; indicating a temporal alignment on the order of the pulse width. The external magnetic field of 20 T was applied using a pulsed Helmholtz coil (few μs in duration, mm length) as described in ref. 28.

The electron density of the plasma was measured using a Mach-Zehnder interferometer with a probe laser (1054 nm wavelength, 650 fs duration) that was propagated perpendicular to the targets and the B-field. The interference fringes were reconstructed using the wavelet algorithm and unwrapping methods of the Neutrino²⁸ analysis tool. The wavelet algorithm provides a synthetic image of the data and this will not match exactly with the experimental data. We calculate the difference in fringe shift between the synthetic image and the data to infer an error bar. This error is then added in quadrature to the error from spatial resolution of the imaging system ($\pm 0.25 \times 10^{16} \text{ cm}^{-2}$).

The proton spectrum was measured with a TP with a 100 μm pinhole placed at a distance of 312 mm from the center of the two foils, with a 50.8 mm long, 0.605 T magnet placed 680 mm from a TR imaging plate on which the ion signals were recorded. The TP was positioned to view a line-of-sight perpendicular to the target irradiated by the L1 beam (shown in Fig. 1). The energy spectra from shots without applied B-field are fitted to exponential laws, $dN/dE d\Omega = (N/T) \exp(-E/T)$, with $N = 10^{13} \text{ sr}^{-1}$, $T = 3.2 \text{ MeV}$ for a single target, and with $N = 2.4 \times 10^{12} \text{ sr}^{-1}$, $T = 1.6 \text{ MeV}$ for a double-target configuration.

Simulations. The PIC simulations were carried out using the PICLS code³⁰. As the geometry of the experiment possessed some symmetry in the direction of the magnetic field, two-dimensional effects are expected to be the most important. Also, to be closer to reality in plasma parameters, sizes and times, a 2D geometry was chosen for the simulation of the whole plasma interaction process.

The simulation box $X_0 \times Y_0$ was $220 \times 250 \mu\text{m}$, or 823×864 cells, with the absorbing boundary conditions in both directions, the time step was 12 fs. We used 200 ions and 200 electrons per cell, with the plasma initial profile

$$n_e(\vec{r}) = n_0 e^{-\left[\frac{(x-x_0)^2}{x_0^2}\right]} F\left(\frac{y-y_0}{\Delta t_0}\right),$$

where, $n_0 = 7 \times 10^{18} \text{ cm}^{-3}$, $\Delta t_0 = 0.2 \text{ ps}$, $F(x) = 1.64 x / v_T e^{-\frac{x^2}{2v_T^2}}$, $v_T = 0.65c$ is the scaling velocity of the TNSA expansion, which corresponds to the proton energy of $\approx 4 \text{ MeV}$, and $y^* = y$ for lower plasma, $y^* = y - Y_0$ for upper plasma. The initial electron distribution was considered to be equivalent to that in both the magnetized and unmagnetized cases. The initial B-field profile is constant. We include only the proton (and not carbon) species as, due to their higher charge-to-mass ratio, these are preferentially accelerated in the TNSA mechanism and also achieve higher velocity so that they make up the majority of the ions present during the interaction time.

The initial electron temperature in the simulations was 100 eV, with a dispersion in the initial positions of the particles. Collisions were turned off in the presented simulations. This simulation setup is relevant to study the TNSA plasma evolution diagnosed in the experiments. In other test PIC simulations with hot electrons, we observed a very transient behavior of the fast/hot electrons that are at the forefront of the TNSA beam, on a timescale $\sim \text{ps}$, in which the static magnetic field can be perturbed. But this is also observed not to impact the longer timescale dynamics investigated here of the TNSA plasma beam (protons and thermalized electrons) which travel much slower than the fast electrons to the central zone between the targets.

Data availability

The data that support the findings of this study are available from the corresponding author upon reasonable request.

Code availability

The PIC code used for the simulations presented in the paper is given in the Methods section and the same is detailed in ref. 30. It is available from the corresponding author upon reasonable request.

Received: 15 January 2019 Accepted: 8 May 2019

Published online: 20 June 2019

References

- Livadiotis, G. *Kappa Distributions: Theory and Applications in Plasmas* (Elsevier, Amsterdam, 2017).
- Decker, R. B. et al. Mediation of the solar wind termination shock by non-thermal ions. *Nature* **454**, 67–70 (2008).
- Park, J., Caprioli, D. & Spitkovsky, A. Simultaneous acceleration of protons and electrons at nonrelativistic quasiparallel collisionless shocks. *Phys. Rev. Lett.* **114**, 085003 (2015).
- Bell, A. The acceleration of cosmic rays in shock fronts. *Mon. Not. R. Astron. Soc.* **182**, 443 (1978).
- Blandford, R. & Eichler, D. Particle acceleration at astrophysical shocks: a theory of cosmic ray origin. *Phys. Rep.* **154**, 1 (1987).
- Spitkovsky, A. Particle acceleration in relativistic collisionless shocks: Fermi process at last? *Astrophys. J. Lett.* **682**, L5 (2008).
- Vink, J. & Laming, J. M. On the magnetic fields and particle acceleration in Cassiopeia A. *Astrophys. J. Lett.* **584**, 758 (2003).
- Martins, S. F., Fonseca, R. A., Silva, L. O. & Mori, W. B. Ion dynamics and acceleration in relativistic shocks. *Astrophys. J. Lett.* **695**, L189 (2009).
- Burgess, D. Particle acceleration at the Earth's bow shock. In *The High Energy Solar Corona: Waves, Eruptions, Particles. Lecture Notes in Physics*, Vol 725 (eds Klein, K. L. & MacKinnon, A. L.) (Springer, Berlin, Heidelberg, 2007).
- Kato, T. & Takabe, H. Nonrelativistic collisionless shocks in weakly magnetized electron-ion plasmas: two-dimensional particle-in-cell simulation of perpendicular shock. *Astrophys. J.* **721**, 828 (2010).
- Hoshino, M. & Shimada, N. Nonthermal electrons at high Mach number shocks: electron shock surfing acceleration. *Astrophys. J.* **572**, 880 (2002).
- Cerutti, B., Uzdensky, D. A. & Begelman, M. C. Extreme particle acceleration in magnetic reconnection layers: application to the gamma-ray flares in the Crab Nebula. *Astrophys. J.* **746**, 148 (2012).
- Liang, E., Nishimura, K., Li, H. & Gary, S. P. Particle energization in an expanding magnetized relativistic plasma. *Phys. Rev. Lett.* **90**, 085001 (2003).
- Paesold, G., Blackman, E. G. & Messmer, P. On particle acceleration and trapping by Poynting flux dominated flows. *Plasma Phys. Control. Fusion* **47**, 1925 (2005).
- Cheung, A. Y., Goforth, R. R. & Koopman, D. W. Magnetically induced collisionless coupling between counterstreaming laser-produced plasmas. *Phys. Rev. Lett.* **31**, 429 (1973).
- Ross, J. et al. Collisionless coupling of ion and electron temperatures in counterstreaming plasma flows. *Phys. Rev. Lett.* **110**, 145005 (2013).
- Morita, T. et al. Interaction of high Mach-number shocks in laser-produced plasmas. *High Energy Density Phys.* **9**, 187 (2013).
- Li, C.-K. et al. Structure and dynamics of colliding plasma jets. *Phys. Rev. Lett.* **111**, 235003 (2013).
- Schaeffer, D. B. et al. Generation and evolution of high-Mach-number laser-driven magnetized collisionless shocks in the laboratory. *Phys. Rev. Lett.* **119**, 025001 (2017).
- Fox, W. et al. Filamentation instability of counterstreaming laser-driven plasmas. *Phys. Rev. Lett.* **111**, 225002 (2013).
- Huntington, C. M. et al. Observation of magnetic field generation via the Weibel instability in interpenetrating plasma flows. *Nat. Phys.* **11**, 173 (2015).
- Ross, J. S. et al. Transition from collisional to collisionless regimes in interpenetrating plasma flows on the national ignition facility. *Phys. Rev. Lett.* **118**, 185003 (2017).
- Allen, M. et al. Direct experimental evidence of back-surface ion acceleration from laser-irradiated gold foils. *Phys. Rev. Lett.* **93**, 265004 (2004).
- Wilks, S. et al. Energetic proton generation in ultra-intense laser-solid interactions. *Phys. Plasmas* **8**, 542 (2001).
- Davis, S. P. et al. Numerical simulations of energy transfer in counterstreaming plasmas. *High Energy Density Phys.* **9**, 231 (2013).
- Tsunehiko, N. & Takabe, H. Nonrelativistic collisionless shocks in weakly magnetized electron-ion plasmas: two-dimensional particle-in-cell simulation of perpendicular shock. *Astrophys. J.* **721**, 828 (2010).
- Higginson, D. P. et al. A novel platform to study magnetized high-velocity collisionless shocks. *High Energy Density Phys.* **17**, 190 (2015).
- Kugland, N. et al. Self-organized electromagnetic field structures in laser-produced counter-streaming plasmas. *Nat. Phys.* **8**, 809 (2012).
- Dromey, B. et al. Picosecond metrology of laser-driven proton bursts. *Nat. Commun.* **7**, 10642 (2016).
- Korneev, Ph, D'Humières, E., Tikhonchuk, V., Higginson, D. P. & Fuchs, J. TNSA-like plasmas collision in an ambient magnetic field as a route to astrophysical collisionless shock observation in a laboratory. *High Energy Density Phys.* **17**, 183 (2015).
- Korneev, Ph, D'Humières, E. & Tikhonchuk, V. Collisionless plasma interpenetration in a strong magnetic field for laboratory astrophysics experiments. *Phys. Plasmas* **21**, 22117 (2014).
- Thomson, J. J. Cathode rays. *Philos. Mag.* **44**, 293 (1897).
- McKenna, P. et al. Characterization of proton and heavier ion acceleration in ultrahigh-intensity laser interactions with heated target foils. *Phys. Rev. E* **70**, 036405 (2004).
- Chen, S. N. et al. Passive tailoring of laser-accelerated ion beam cut-off energy by using double foil assembly. *Phys. Plasmas* **21**, 023119 (2014).
- Ziegler, J. F., Biersack, J. P. & Ziegler, M. *SRIM*. <http://www.lulu.com/content/1524197> (2008).
- Sarri, G. et al. Dynamics of self-generated, large amplitude magnetic fields following high-intensity laser matter interaction. *Phys. Rev. Lett.* **109**, 205002 (2012).

37. Albertazzi, B. et al. Dynamics and structure of self-generated magnetic fields on solids following high contrast, high intensity laser irradiation. *Phys. Plasmas* **22**, 123108 (2015).
38. Antici, P. et al. Hot and cold electron dynamics following high-intensity laser matter interaction. *Phys. Rev. Lett.* **101**, 105004 (2008).
39. Zaqarashvili, T. V., Vörös, Z., Narita, Y. & Bruno, R. Twisted magnetic flux tubes in the solar wind. *Astrophys. J. Lett.* **783**, L19 (2014).
40. Reale, F. et al. 3D MHD modeling of twisted coronal loops. *Astrophys. J.* **830**, 21 (2016).

Acknowledgements

The authors thank S. Andrews, J. Bonlie, C. Bruns, R. C. Cauble, D. Cloyne, R. Costa and the entire staff of the Titan Laser and the Jupiter Laser facility for their support during the experimental preparation and execution, and T. Grismayer, K. Schoeffler, L.O. Silva for discussions. This work was supported by ANR Blanc Grant No. 12-BS09-025-01 SILAMPA and by the Russian Foundation for Basic Research (grants #18-29-21029 and #18-02-00850). It has been carried out within the framework of the EUROfusion Consortium and has received funding from the European Union's Horizon 2020 research and innovation programme through the ToIFE program (Grant Agreement No. 633053) and through the European Research Council (ERC, Grant Agreement No. 787539). The views and opinions expressed herein do not necessarily reflect those of the European Commission. It has received funding from Laserlab-Europe (H2020 EC-GA 654148), and was partly done within the LABEX Plas@Par project, which is supported by Grant No. 11-IDEX-0004-02 from Agence Nationale de la Recherche. This work was supported by the MEPhI Academic Excellence Project (Contract No. 02.a03.21.0005, 27.08.2013). This work was performed under the auspices of the U.S. Department of Energy by Lawrence Livermore National Laboratory under Contract DE-AC52-07NA27344. This work was granted access to the HPC resources of CINES under the allocations 2016-056129 and 2017-056129 made by GENCI (Grand Equipement National de Calcul Intensif). A part of the numerical calculations was presented at Joint Supercomputer Center of the Russian Academy of Sciences and resources of NRNU MEPhI high-performance computing center. The work was also done in the frame of state assignment of Ministry for Science and Higher Education of Russia to JIHT RAS (topic #01201357846). The research leading to these results is supported by Extreme Light Infrastructure Nuclear Physics (ELI-NP) Phase I, a project co-financed by the Romanian Government and European Union through the European Regional Development Fund.

Author contributions

J.F. and E.d'H. conceived the project. D.P.H., R.R., B.P., S.N.C., J.B., H.P., S.P., and J.F. performed the experiment, with support from R.S., and M.S. D.P.H., R.R., and J.F. analyzed the data. E.d'H., P.K., C.Ru., and Q.M. developed the theoretical frame and performed the main simulations, with support from A.G., M.G., L.G., F.P., C.Ri., T.V., and V.T. J.F., D.P.H., E.d'H., P.K., and Q.M. wrote the bulk of the paper. All authors commented the paper at its various stages.

Additional information

Supplementary information accompanies this paper at <https://doi.org/10.1038/s42005-019-0160-6>.

Competing interests: The authors declare no competing interests.

Reprints and permission information is available online at <http://npg.nature.com/reprintsandpermissions/>

Publisher's note: Springer Nature remains neutral with regard to jurisdictional claims in published maps and institutional affiliations.



Open Access This article is licensed under a Creative Commons Attribution 4.0 International License, which permits use, sharing, adaptation, distribution and reproduction in any medium or format, as long as you give appropriate credit to the original author(s) and the source, provide a link to the Creative Commons license, and indicate if changes were made. The images or other third party material in this article are included in the article's Creative Commons license, unless indicated otherwise in a credit line to the material. If material is not included in the article's Creative Commons license and your intended use is not permitted by statutory regulation or exceeds the permitted use, you will need to obtain permission directly from the copyright holder. To view a copy of this license, visit <http://creativecommons.org/licenses/by/4.0/>.

© The Author(s) 2019